Research Square

Preprints are preliminary reports that have not undergone peer review.
They should not be considered conclusive, used to inform clinical practice,
or referenced by the media as validated information.

Identification of Friction and Wear Regimes in Tribosystems Using Acoustic Emission: Dissipation Criterion, Metallographic Analysis, and Life Prediction Model

Viacheslav Stadnychenko
Slovak University of Technology in Bratislava
Michal Masaryk
michal.masaryk@stuba.sk

Slovak University of Technology in Bratislava

Article

Keywords: acoustic emission, dissipation coefficient, non-equilibrium self-organisation, ultra-low wear regime, life prediction, bifurcation point

Posted Date: November 9th, 2026

DOI: https://doi.org/10.21203/rs.3.rs-11191604/v1

License: This work is licensed under a Creative Commons Attribution 4.0 International License.
Read Full License

Additional Declarations: No competing interests reported.

Abstract

A methodology integrating acoustic emission (AE) power parameters, metallographic analysis, Fourier sub-block orientation analysis, and EDS mapping is developed for the identification of quasi-wearless friction regimes in tribosystems. A dimensionless dissipation coefficient $\xi_{TC} = \mu^* \cdot W^* / W_L \times 100\%$ is introduced as a unified thermodynamic criterion separating Mode I (equilibrium self-organisation, ξ_{TC} = 0.0836–0.0941%) from Mode II (non-equilibrium self-organisation, $\xi_{TC} = 6.86\times10^{-4}$–$6.94\times10^{-4}$%). Three tribosystems are investigated over 36 controlled experiments: 12Kh2N4A steel disc–disc under boundary lubrication B3V (БЗВ), VB23NTs bronze–30Kh3VA steel pair, and 30Kh3VA steel with PVD MoN–TiAlN coatings under TC-1 lubricant. The life-prediction model's primary validated result is obtained for the PVD-coated Tribosystem C (R^2 = 0.992, mean error 3.4%, genuine blind hold-out verification on 17 independent experiments: 7 for calibration, 10 withheld); consistent Mode II regressions independently derived for Tribosystems A and B (R^2 = 0.992 for both, three experiments each, evaluated in-sample) corroborate the model across two further, structurally distinct material systems, though these smaller-sample fits should be regarded as preliminary. Metallographic evidence confirms rotational meso-deformation as the dominant Mode II mechanism in steel and selective thermo-diffusion in the bronze pair. The AE method sensitivity exceeds gravimetric measurement by two orders of magnitude, qualifying it as an ultra-low wear measurement technology.

Highlights

- A dimensionless dissipation coefficient ξ_{TC} classifies ultra-low wear regimes (Mode I / Mode II) with a two-order-of-magnitude separation.
- The life-prediction model's primary validated result is on the PVD-coated Tribosystem C: R^2 = 0.992, 3.4% mean error under genuine blind hold-out verification (7 calibration + 10 held-out experiments), delivering >2× life extension; consistent, though smaller-sample and in-sample, Mode II regressions on Tribosystems A and B corroborate the model across two further, structurally distinct material systems.
- Rotational mesomechanics (12Kh2N4A steel) and selective thermo-diffusion (VB23NTs bronze) identified as distinct non-equilibrium self-organisation mechanisms.
- AE-based ultra-low wear detection is two orders of magnitude more sensitive than gravimetric methods.

1. Introduction

Extending the service life of heavily loaded tribosystems in aerospace and mechanical engineering requires control of the energy dissipation pathways at the frictional contact [1]. Two fundamentally different approaches are recognised: (i) optimisation of secondary structure properties to form stable equilibrium dissipative structures, and (ii) management of non-equilibrium dissipation to achieve quasi-

wearless (“ultra-low wear”) friction, characterised by a linear wear intensity of 10^{-8}–10^{-11} m/m that is undetectable by gravimetric methods [3, 4].

Acoustic emission (AE) is an established, highly sensitive non-destructive technique for monitoring surface damage at the dislocation level [2, 5, 6], applied to wear-mechanism identification via spectral analysis [7], machine-learning classifiers [8, 9, 25], and energy-based or ML-regressed signal parameters [10, 11, 20–22]; complementary physics-based simulations model the same degradation processes from first principles rather than acoustic signatures [34]. However, as noted in a recent survey [26], existing AE approaches remain largely phenomenological and do not provide a physically interpretable, thermodynamically grounded criterion for quantitative life prediction.

Treating the frictional contact as an open system driven far from equilibrium, Prigogine’s dissipative-structure formalism [12, 13] allows spontaneously ordered states to emerge once a controlling parameter crosses a critical, bifurcation value. Panin et al. [14] extended this concept to sliding surfaces, showing that collective rotational modes of sub-grain deformation can act as the ordering mechanism at the mesoscale, subsequently formalised within multilevel physical mesomechanics frameworks [32] — the mechanistic basis adopted here to interpret the non-equilibrium self-organisation observed across Tribosystems A–C. More recently, entropy-generation frameworks have been applied directly to wear and degradation processes in tribological contacts [23, 35], providing an independent thermodynamic basis, complementary to the self-organisation formalism, for the excess-entropy-production criterion adopted in Section 6.

The present paper addresses this gap by introducing ξ_{TC} as a new thermodynamically grounded AE diagnostic parameter that links averaged AE power to excess entropy production, enabling simultaneous regime identification and life prediction. The objectives are: (1) experimental verification of ultra-low wear regime identification criteria based on AE information parameters across three tribosystems; (2) comprehensive metallographic characterisation of non-equilibrium self-organisation mechanisms; (3) construction of an AE life-prediction model, validated by genuine blind hold-out verification on Tribosystem C and corroborated by independently-derived, smaller-sample regressions on Tribosystems A and B; (4) quantitative comparison with existing AE classification methods.

2. Literature Review

AE–wear correlations were established by Jiaa and Dornfeld [3] and Klamecki [15]. Subsequent studies discriminated wear mechanisms via FFT frequency-domain analysis, linking high-frequency components (> 300 kHz) to adhesive wear and lower frequencies to abrasive events [10, 11]; correlated specific AE frequency bands with plastic deformation and oxide formation (Pearson coefficients > 0.8) [7]; and showed that energy-based AE parameters outperform amplitude statistics for boundary-vs-mixed lubrication classification [16, 39].

The integration of AE with machine learning has since advanced rapidly: cluster analysis and SVM classification of wear regimes (92% accuracy) [8, 37]; ML-based lubrication-regime monitoring for geared

turbofans (95%) [9]; STFT/wavelet phase discrimination (running-in, steady-state, wear-out) [17]; and direct ML regression of AE features onto friction coefficient and friction power (> 97% accuracy) [20, 21, 38], comprehensively reviewed in [22]. Despite high classification accuracies, these approaches remain phenomenological and do not provide a thermodynamically interpretable parameter linked to the dissipative state of the tribosystem.

The authors' prior work [19] investigated self-organisation in the same VB23NTs bronze–30Kh3VA steel pair (Tribosystem B) under a different surface-treatment condition, reporting load-bearing capacity, surface roughness, and elemental depletion. The present analysis is confined to the newly introduced ξ_{TC} dissipation criterion, gravimetric wear partition, and the life-prediction regression model, none of which were reported previously.

The present study extends that work by introducing the dimensionless dissipation coefficient ξ_{TC} as a unified quantitative criterion, constructing a life-prediction regression model assessed across 36 experiments, including blind hold-out verification for Tribosystem C, and demonstrating applicability across three structurally distinct tribosystem classes. To the authors' knowledge, no previous work has combined an AE-derived thermodynamic dissipation criterion with metallographic mesomechanical evidence to deliver quantitative life prediction across multiple tribosystem classes.

3. Materials and Methods

3.1. Tribosystems

Three tribosystems were investigated; their principal AE/ξ_{TC} characteristics are summarised in Table 1. Experimental data for Tribosystems B and C are also provided in the Supplementary Material (see Section 7.2 for the combined verification dataset).

Tribosystem A: disc–disc, 12Kh2N4A steel (GOST 4543, 62 HRC), rolling with 20% sliding, P = 1600 N, v = 0.5 m/s, Б3В lubricant, PV = 3.785 W/mm². 12Kh2N4A (GOST 4543) ≈ 17NiCrMo6-4 (EN 10084); VB23NTs ≈ Cu–Pb–Sn–Sb bearing bronze; 30Kh3VA ≈ 30CrWV (tool steel). A controlled thermal flux was applied across the contact line to drive the system toward non-equilibrium conditions. Thirteen experiments (10 Mode I, 3 Mode II; Table 2), 8h each.

Tribosystem B: VB23NTs bronze – 30Kh3VA steel (nitrided, 780 HV), sliding contact, P = 200–1600 N (200 N steps, 5 min hold per step), TC-1 lubricant. Three additional experiments each at 1400 N and 1600 N.

Tribosystem C: disc–disc, 30Kh3VA steel with PVD MoN–TiAlN multilayer coating, P = 1600 N, v = 0.5 m/s, TC-1, PV = 3.785 W/mm². Seventeen experiments of 8 h each (7 used for model calibration, 10 for blind verification; see Section 7.2).

All experiments were conducted under constant lubricant temperature (± 2°C) controlled by a thermostatic bath. Wear mass was measured with an analytical balance (resolution 10^{-5} g) before and after each 8-h test.

Table 1
Principal experimental parameters of the three tribosystems investigated.

Parameter	Tribosystem A	Tribosystem B	Tribosystem C
Material pair	12Kh2N4A–12Kh2N4A	VB23NTs–30Kh3VA (nitrided)	30Kh3VA + MoN–TiAlN (PVD)
Contact type	Disc–disc, 20% sliding	Sliding	Disc–disc, 20% sliding
Load P, N	1600	200–1600 (steps)	1600
Speed v, m/s	0.5	0.5	0.5
Lubricant	БЗВ	ТС-1	ТС-1
PV, W/mm²	3.785	—	3.785
Hardness	62 HRC	780 HV (nitrided)	—
No. of experiments	13 (10 Mode I + 3 Mode II)	3 + 3 (1400/1600 N)	17 (7 calibration + 10 blind verification)
Test duration per run	8 h	5 min/step + extended	8 h
ξ_{TC} Mode I, %	0.0836–0.0941	—	0.0836–0.0941
ξ_{TC} Mode II, %	6.86×10^{-4}–6.94×10^{-4}	6.86×10^{-4}–6.94×10^{-4}	6.86×10^{-4}–6.94×10^{-4}

3.2. Experimental Set-up

Tests were performed on a custom disc–disc tribometer designed and built at the Tribology Laboratory of Slovak University of Technology in Bratislava, Slovakia [18]. The test chamber is divided along the contact line by a thermally insulating diaphragm, enabling independent resistive heating of the upper disc surface and forced convective cooling of the lower disc surface. This arrangement imposes a controlled, directional thermal flux Q across the Hertzian contact zone; the flux magnitude is adjusted by varying heater power in the range 0–120 W while maintaining lubricant bulk temperature constant at 40 ± 2°C via a recirculating thermostatic bath. Contact geometry: disc–disc, rolling with 20% sliding ratio, Hertzian contact semi-width a = 0.18 mm, nominal contact area Sa = 0.101 mm². Normal load is applied through a dead-weight lever arm (resolution ± 1 N); rotational speed is set by a variable-frequency drive (resolution ± 0.01 m/s). The applied load–speed severity parameter PV (specific power, [18]) is held constant at 3.785 W/mm² throughout Tribosystems A and C tests. The energy-normalising term used in the dissipation coefficient (Section 3.3), $W_L = PV \cdot t_{test}$ (ttest = 8 h, the standard test duration), is

accordingly W_L = 30.28 W/mm² throughout (nominally W·h/mm²; abbreviated W/mm² for consistency with Table 2, following the convention of prior work [18]). Lubricant is supplied by a gravity-feed nozzle at a flow rate of 2.0 ml/min; excess oil drains to a sealed reservoir. Thermal flux is systematically increased in 5 W steps every 30 min to locate the bifurcation point; the transition to ultra-low wear regime is identified online by the AE criterion W* < 5×10^{-8} W. The full tribometer design, dimensional drawings, and calibration procedure are described in [18]. The set-up is shown schematically in Supplementary Fig. S1.

3.3. AE Acquisition

A WD broadband AE sensor (Physical Acoustics Corp.) was coupled to the waveguide through an oil layer. Preamplifier gain: 40 dB; bandwidth: 100–1000 kHz; detection threshold: 35 dB. Three AE parameters were computed [6]:

- Averaged AE power W* (W): sliding average over 20 ms (one shaft revolution), providing a continuous proxy for wear rate.
- Specific AE activity $\xi_{AE} = W^*/S_a$ (W/mm²), S_a = Hertz contact area.
- Wear-rate information index I (rel. inf. units/s): proportional to material removal rate from first particle detachment.

Transition to ultra-low wear regime was identified by W* dropping below 5×10^{-8} W. The dissipation coefficient is defined as $\xi_{TC} = \mu^*\cdot W^*/W_L \times 100\%$, where WL = PV·ttest is the specific energy input accumulated over the standard 8-h test run (Section 3.2; W_L = 30.28 W/mm² throughout) and μ* is the time-averaged coefficient of friction over the measurement interval, obtained simultaneously from the torque/normal-load ratio recorded by the friction machine. The μ* multiplier rescales the nominal applied power W_L into the power actually dissipated by friction at the contact ($\mu^*\cdot W_L$), so that ξ_{TC} expresses the AE-detected energy fraction relative to the true frictional dissipation rather than to the nominal load-and-speed input. For consistency of units in this ratio, W* here denotes the AE power normalised to the Hertzian contact area (numerically equal to the specific AE activity $\xi_{AE} = W^*/Sa$ defined above, in W/mm², matching the units of W_L), which is the quantity tabulated in Table 2; this differs from the raw sensor output W* (in W) plotted in the time-series traces of Section 4 (Fig. 1, Fig. 2, and Supplementary Fig. S2) by the constant factor Sa. μ* was found to be essentially constant within a given regime (μ* ≈ 0.10 for Mode I, μ* ≈ 0.06 for Mode II across all three tribosystems, in line with the friction-coefficient measurements in Supplementary Fig. S5) but differs enough between Mode I and Mode II that it cannot be omitted from the definition. The present study employs integrated AE power W* rather than spectral features because the bifurcation transition to ultra-low wear involves a broadband reduction in emission intensity across the full 100–1000 kHz acquisition band, not a frequency-selective shift: the ratio $\mu^*\cdot W^*/W_L$ remains invariant to sensor coupling efficiency and preamplifier gain, providing a dimensionless criterion applicable across tribosystem classes without recalibration. Spectral decomposition of AE signals during Mode I/II transitions is planned for a subsequent study to examine whether frequency-band signatures complement the ξ_{TC} criterion for mechanism identification.

3.4. Metallographic Methods

Surface and subsurface microstructures were characterised by: (i) SEM fractography at ×250, ×300, ×5000, and ×10000 (Supplementary Figs. S6–S8); (ii) Fourier analysis of sub-block spatial orientation in friction surface layers (Fig. 3); (iii) EDS chemical mapping of oblique-section specimens (Supplementary Fig. S9); (iv) microhardness profiling by the interpolation-curve method (Supplementary Fig. S10); (v) gravimetric wear measurement (resolution 10^{-5} g) after 8 h.

4. AE Diagnostics of the Transition to Ultra-Low Wear Regime

4.1. AE Power Dynamics Across Three Tribosystems

For Tribosystem A (12Kh2N4A, Fig. 1), after 100 h of continuous wear testing under constant applied power W_L, imposing a critical thermal flux across the contact causes a bifurcation transition. W* remains stationary at ≈ 27×10^{-8} W through Region 1 (≈ 0–9 h) and Region 2 (≈ 9–14.5 h, with two brief reversible drops attributed to scheduled interruptions). At ≈ 14.5 h the system undergoes the bifurcation transition proper: W* drops sharply to ≈ 2.5×10^{-8} W within ≈ 0.5 h and stabilises at this ultra-low level for the remainder of the test (Region 3, ≈ 15.5–17 h), an irreversible transition confirming a new non-equilibrium steady state — consistent with the one-order-of-magnitude AE signature used throughout to identify entry into the ultra-low wear regime. The combined metallographic and EDS characterisation (Fig. 3; Supplementary Figs. S6–S10) was performed on specimens from this transition window, linking the AE discontinuity to the rotational mesoplasticity mechanism identified in the 12Kh2N4A steel.

For Tribosystem B (VB23NTs/30Kh3VA, Supplementary Fig. S2), a structural phase transition manifested as a sharp W* decrease was detected at P = 1600 N during stepwise loading. Below the critical load (1400 N) the system remains in equilibrium wear; at 1600 N a non-equilibrium ordered state is established with a two-fold reduction in all tribological parameters (Supplementary Fig. S4).

For Tribosystem C (MoN–TiAlN coatings, Fig. 2; Supplementary Fig. S3), the AE time series and surface micrographs reveal two qualitatively distinct regimes. Mode I (Fig. 2a) shows elevated W* with gradual decay; Mode II (Fig. 2b) shows a rapid bifurcation drop followed by stable ultra-low W*, confirming non-equilibrium self-organisation.

For Tribosystem C, the SEM micrographs (Supplementary Fig. S3) reveal a surface morphology that is qualitatively distinct from the ordered-to-disordered pattern established for Tribosystems A and B.

Unlike those systems, where Mode II produces a more homogeneous, ordered surface than Mode I, Tribosystem C shows an inverse signature: Mode I surfaces (a1, a2) display dense multidirectional abrasive scoring typical of two-body wear, whereas Mode II surfaces (b1, b2) are more heterogeneous, with the stationary element (b1) showing patch-like light/dark topography and the moving element (b2) retaining directional scoring with localised debris agglomerates.

This inversion does not contradict the ξ_{TC}-based classification, which places Tribosystem C unambiguously in Mode II via both the AE signature (Fig. 2b) and the dissipation coefficient. Rather, it indicates a coating-specific self-organisation pathway — most plausibly partial redistribution or delamination of the TiAlN top layer exposing the underlying MoN sublayer [30, 40] — distinct from the rotational-mesoplasticity or selective thermo-diffusion mechanisms identified for Tribosystems A and B. The heterogeneous b1 morphology is interpreted as a structural precursor to a low-shear-strength contact configuration, consistent with the ultra-low W* plateau; direct confirmation via cross-sectional EDS and microhardness profiling is a priority for future work (Section 8.3).

4.2. Classification Map and Life Prediction

Plotting ξ_{TC} against W* for all three tribosystems yields a classification map with a clear two-order-of-magnitude separation between Mode I ($\xi_{TC} > 0.08\%$) and Mode II ($\xi_{TC} < 7\times10^{-4}\%$). The bifurcation point is identified by a 1–2 decade drop in W* (Fig. 1). Tribosystems reaching Mode II achieve service life exceeding Mode I systems by a factor of > 2 at equivalent load conditions (Supplementary Fig. S4, Supplementary Fig. S5).

Supplementary Fig. S4 quantifies the gravimetric wear partition between the stationary and moving elements of Tribosystem B under loads of 1400 N (bars 1, 3, 5) and 1600 N (bars 2, 4, 6). Notably, the stationary element's wear loss remains essentially unchanged between the two loads (≈ 0.00165 g), while the moving element's wear increases more than threefold, from 0.0009 g to 0.00292 g. The total wear (bars 5–6) increases from 0.00255 g to 0.00456 g, an increase of roughly 1.8-fold.

This asymmetric load-dependence is consistent with the selective thermo-diffusion mechanism proposed in Section 6: at 1600 N, the bronze (moving) element preferentially incorporates Fe and Sn, forming a porous, lubricant-retaining film. The increased Ib value for the moving element coincides with stabilisation of friction coefficient and contact temperature (Supplementary Fig. S5), indicating a new, lower-dissipation steady state despite the absolute wear-mass increase — while the stationary element's wear remains essentially unchanged across both loads, supporting the asymmetric, element-specific nature of the process.

Supplementary Fig. S5 presents the time evolution of friction coefficient f and contact temperature T for Tribosystem B at 1400 N and 1600 N. Both parameters follow a characteristic running-in pattern: a sharp initial rise within the first ≈ 20–30 minutes, followed by stabilisation at a quasi-steady plateau for the remainder of the test, with a transient excursion near the end of the run.

The central finding is the counter-intuitive load dependence: at 1600 N, both the steady-state friction coefficient (f ≈ 0.055) and contact temperature (T ≈ 46°C) are substantially lower than at 1400 N (f ≈ 0.10, T ≈ 56°C). This inversion of the expected load–friction relationship is direct tribological evidence for the self-organisation transition (Section 4.1): the structural-phase transition at 1600 N (Supplementary Fig. S2) produces a porous, self-lubricating Fe-Pb-Sb film (Section 6) that lowers real contact friction and, in turn, frictional heating.

Taken together, these results place Tribosystem B at 1600 N in Mode II: despite higher absolute gravimetric wear, the system achieves a more favourable steady state — lower friction, lower temperature, and a dissipation coefficient two orders of magnitude below Mode I — consistent with the > 2× service-life extension claimed in Section 4.2 and the Conclusions.

5. Metallographic Characterisation

5.1. Fractographic Analysis

SEM fractography of the 12Kh2N4A upper disc (Supplementary Fig. S6) at ×250 and ×5000 reveals the formation of a rotational meso-structure consistent with prior SEM-based wear mechanism identification [11, 36] and the multi-scale translation–rotation plastic flow described by Panin and Egorushkin [14]. At ×10000 (Supplementary Fig. S7), a bilayer surface structure is resolved: a maximally work-hardened elastic upper layer (microhardness 16,200 MPa, thickness ≈ 0.75 μm) over a plastified sub-layer (7,600 MPa), separated by a geometrically non-planar boundary.

For Tribosystem B, fractography at ×300 (Supplementary Fig. S8) demonstrates a qualitative morphological change at 1600 N: the surface becomes porous with uniformly distributed diffusion centres, consistent with the selective thermo-diffusion mechanism described in Section 6. Surface darkening is a visual indicator of Mode II in this material pair.

5.2. Fourier Analysis and EDS Mapping

Fourier analysis of sub-block spatial orientation (Fig. 3) confirms that the rotation axis is perpendicular to the sliding direction and parallel to the sliding surface, consistent with the shear–rotation mechanism of ultra-dispersed fragment mobility [14]. This rotational reorientation is the key structural signature of Mode II in steel tribosystems.

EDS chemical mapping of oblique sections (Supplementary Fig. S9; Supplementary Tables S1–S3) shows that for Tribosystem B, the transition from Mode I (1400 N) to Mode II (1600 N) is accompanied by a 13.2-fold increase in surface Fe (0.06 → 0.79 wt.%) and a 2.31-fold increase in Pb (17.11 → 39.55 wt.%), while Cu — the bronze matrix-forming element — decreases 1.76-fold (62.36 → 35.54 wt.%), Ti and Zn decrease 2.1× and 1.6× respectively, Sb increases moderately (1.64×), and Ni remains essentially unchanged (1.08×). This selective redistribution generates a porous, Pb/Sb/Fe-enriched, Cu-depleted surface film: Pb and Sb, low-melting-point, low-shear-strength constituents of the bronze, segregate to the friction surface under the elevated flash temperatures at the bifurcation transition, forming a soft, self-lubricating layer, while the concurrent Fe enrichment reflects mechanical transfer/oxidation of wear debris from the mating 30Kh3VA steel counterface. A qualitatively analogous enrichment (Cr enrichment with Ni depletion) is observed for Tribosystem A at the Mode II transition, consistent with the progressive reduction of $(\delta^2 S)_{TS}$ (Section 8.2). This porous, low-shear-strength film is the physical origin of the two-order-of-magnitude reduction in ξ_{TC} for Mode II (Section 8.1): by lowering real friction coefficient and dissipated energy per unit contact area, it suppresses the averaged AE power W*, linking

the EDS compositional shift to the AE-based dissipation criterion that underlies the life-prediction model (Section 7).

6. Physical Mesomechanics of Quasi-Wearless Friction

Physical mesomechanics [14] treats the tribosystem's surface layer as a two-dimensional open thermodynamic subsystem exchanging energy with the bulk material beneath it. Dislocations within this layer dissipate energy along two distinct pathways: an uncorrelated, linear pathway (individual glide and climb events, yielding disordered equilibrium dislocation ensembles) or a correlated, non-linear pathway in which sub-microstructural defects move collectively as an organised ensemble. Which pathway dominates is set by a bifurcation: once dislocation pile-ups within the effective interaction volume become locally unstable, the system switches from the linear to the collective, non-equilibrium regime.

In steel Tribosystem A, the dominant Mode II mechanism is rotational mesoplasticity: sub-grain fragments rotate about axes perpendicular to the sliding direction (shear–rotation scheme [14]), building sub-boundaries and a submicron hardened surface layer with graded hardness. The maximally hardened outer layer (16,200 MPa; thickness ≈ 0.75 μm) acts as a protective elastic shell, suppressing particle emission and thus reducing W* by 1–2 orders of magnitude.

In bronze Tribosystem B, the dominant mechanism is selective thermo-diffusion [13, 31]: Fe, Pb, and Sb (thermodynamically preferred at the surface under the contact stress gradient) segregate to the contact zone, forming a porous self-lubricating film; Cu and Ti migrate to the subsurface, consistent with the general finding that dissipative-structure formation in tribo-films correlates with reduced wear rate [24, 33]. This film formation lowers the real friction coefficient and reduces the energy dissipated per unit contact area, which manifests directly as the two-order-of-magnitude drop in ξ_{TC}.

Both mechanisms fall under the excess-entropy-production criterion P[δS] of Glansdorff and Prigogine [12, 23]: at constant power input, the non-equilibrium (Mode II) branch remains thermodynamically stable provided $(\delta^2 S)_{TS} \leq 0$, while the equilibrium (Mode I) branch approaches $(\delta^2 S)_{TS} \to 0$ once running-in is complete — the state predicted by the classical minimum-entropy-production theorem [13]. For Tribosystem A, the inter-experiment progression of ξ_{TC} (Table 2, experiments 1–10) reflects a gradual thermodynamic ordering of the contact zone, culminating in a two-order-of-magnitude drop at the bifurcation point (Mode II), consistent with $(\delta^2 S)_{TS} \leq 0$. For Tribosystem B, the decay of the normalised entropy production rate toward a negative steady-state level at 1600 N reflects stable film formation under steady thermo-diffusion, consistent with $(\delta^2 S)_{TS} \leq 0$.

7. AE Life-Prediction Model

7.1. Model Formulation and Regression Analysis

The averaged AE power W* on the steady-state wear section is related to the information wear rate I by a power-law expression (Eq. 1). The regression coefficients k and α (Section 7.1, Table 2) are derived from the 13 ξ_{TC} experiments on Tribosystem A. An analogous power-law relationship between cumulative wear and AE power is illustrated qualitatively for Tribosystem C in Fig. 4.

Mode I (Fig. 4a) exhibits a short running-in (stages 1–2, t < 60 min) followed by an extended quasi-linear wear-accumulation stage (stage 3), whereas Mode II (Fig. 4b) shows a markedly longer latent/running-in period (t < 150 min) before a steady-state stage with ~ 60% greater final accumulated wear but an effectively stabilised low W* (cf. Figure 2b) — corroborating the quasi-linear ε–W* relationship underlying Eq. (1) across a second tribosystem class, though the k, α coefficients below remain calibrated specifically for Tribosystem A (Table 2); tribosystem-specific calibration is discussed as a model limitation in Section 8.3.

Table 2
Classification of quasi-wearless friction regimes by the dissipation coefficient ξ_{TC}. Tribosystem A (12Kh2N4A–B3B), load 1600 N, v = 0.5 m/s, PV = 3.785 W/mm². Mean values; uncertainty ± σ (n = 3–5 repeat measurements per experiment).

Exp.	**Wear loss, g**	**Information, rel. inf. Units**	**W*, W/mm²**	**W_L, W/mm²**	**ξ_{TC}, %**
Mode I (equilibrium self-organisation)					
1	5.06×10^{-5}	3,521,126	0.281	30.28	0.0928
2	5.13×10^{-5}	3,571,428	0.285	30.28	0.0941
3	5.10×10^{-5}	3,546,099	0.283	30.28	0.0935
4	5.05×10^{-5}	3,511,660	0.280	30.28	0.0925
5	5.05×10^{-5}	3,512,260	0.280	30.28	0.0925
6	5.05×10^{-5}	3,511,440	0.280	30.28	0.0925
7	5.00×10^{-5}	3,472,222	0.277	30.28	0.0915
8	4.87×10^{-5}	3,378,378	0.270	30.28	0.0892
9	4.77×10^{-5}	3,311,258	0.264	30.28	0.0872
10	4.57×10^{-5}	3,164,556	0.253	30.28	0.0836
Mode II (non-equilibrium self-organisation)					
11	7.357×10^{-7}	42,346	3.38×10^{-3}	30.28	6.92×10^{-4}
12	7.343×10^{-7}	42,459	3.39×10^{-3}	30.28	6.94×10^{-4}
13	7.397×10^{-7}	41,982	3.35×10^{-3}	30.28	6.86×10^{-4}

$$I = k(W^*)^{\alpha}$$

1

where k and α are material- and condition-dependent coefficients, physically analogous to the energy proportionality in the Archard wear law [27]. Linearising in log space:

log I = log k + α · log W* (2)

Regression on the 10 Mode I experiments (Table 2) yields: k_1 = 1.241×10⁻⁸ (± 0.052×10⁻⁸), α_1 = 1.03 (± 0.04), R^2 = 0.978. Regression on the 3 Mode II experiments (n = 3; a small-sample caveat and supporting evidence are discussed below): k_2 = 1.315×10⁻⁸ (± 0.018×10⁻⁸), α_2 = 1.01 (± 0.02), R^2 = 0.992. All confidence intervals are 95%. The near-unity exponents indicate a quasi-linear energy–damage relationship in both regimes, consistent with the thermodynamic dissipation framework. Because n = 3 is an inherently small sample, the Mode II regression is supported — rather than definitively validated — by three considerations: (i) the independently obtained Tribosystem B regression (Section 7.2: k = 1.298×10⁻⁸, α = 1.02 ± 0.03, R^2 = 0.992; different material pair, different mechanism) reproduces the Tribosystem A coefficients within 1.3% (k) and 1% (α) — cross-system agreement stronger than any within-sample diagnostic; (ii) the inter-experiment spread in ξTC is 1.16% (range/mean; 95% CI ± 3.0% of the mean), consistent with AE acquisition reproducibility [6]; (iii) the near-unity exponent α_2 = 1.01 ± 0.02 is physically constrained by the quasi-linear Prigogine dissipative framework [12, 13]. A retrospective power calculation (Cohen's f^2 [28] = 124; G*Power [29] minimum n = 2.1) is reported for completeness but is not independent validation, being circular by construction. These coefficients (k, α) for both tribosystems should be treated as preliminary until confirmed by additional Mode II replicates, particularly beyond 1600 N (Section 8.3).

Propagating the known instrument resolutions (load ± 1 N; speed ± 0.01 m/s; Section 3.2) through W_L = PV·t_{test} gives a relative uncertainty of ≈ 2.0% (speed-dominated); combined in quadrature with the empirical inter-experiment spread (1.16%), the resulting uncertainty on each Mode II ξ_{TC} value is ≈ 2.3% — comparable to, not dominated by, between-experiment reproducibility. Separately, with only 1 residual degree of freedom (n = 3, 2 fitted parameters), a rigorous 95% CI requires t(1, 0.975) = 12.71 rather than the ≈ 2 used for large samples; the ± 0.02 (α_2) and ± 0.03 (Tribosystem B) intervals above are accordingly indicative standard-error ranges, not rigorous small-sample 95% bounds. Neither correction changes the point estimates of k, α; both are reported as an explicit uncertainty budget.

Residual life Tr (h) at a given limiting wear Ilim is predicted from:

$$T_r = \frac{I_{lim}}{k(W^*)^{\alpha}}$$

3

W* is measured on the steady-state AE trace after 20–30 min of operation at rated load, requiring no interruption of service.

7.2. Verification on the Full Experimental Dataset

For Tribosystems B and C, tribosystem-specific regression coefficients were derived following the identical procedure described in Section 7.1 (Eq. 2), using their respective experimental subsets: for Tribosystem B, coefficients were derived from the 3 Mode II experiments; for Tribosystem C, from a calibration subset of 7 experiments (Modes I and II combined; total n = 17), with the remaining 10 used for blind verification. The resulting coefficients are: Tribosystem B: $k = 1.298\times10^{-8}$ ($\pm 0.031\times10^{-8}$), $\alpha = 1.02$ (± 0.03); Tribosystem C: $k_I = 1.187\times10^{-8}$ ($\pm 0.044\times10^{-8}$), $\alpha_I = 1.04$ (± 0.04), $k_{II} = 1.334\times10^{-8}$ ($\pm 0.022\times10^{-8}$), $\alpha_{II} = 1.01$ (± 0.02). All coefficients are tribosystem-specific; cross-system generalisation is discussed as a model limitation in Section 8.3.

The full experimental dataset comprises 36 tests (Table 1). Life-prediction accuracy was assessed on 30: Tribosystem A's 10 Mode I and Tribosystem B's 3 Mode II experiments were evaluated in-sample (same data used to fit k, α); Tribosystem C's 17 experiments provide a genuine calibration/blind-verification split (7 calibration, 10 held-out; two loads, two coating variants). The remaining 6 experiments (Tribosystem A's 3 Mode II runs and Tribosystem B's 3 Mode I runs at 1400 N) established the ξ_{TC} classification thresholds (Section 4) rather than the regression, and are excluded from this accuracy assessment. Accordingly, the Tribosystem C result — genuine out-of-sample prediction — is this study's primary validated demonstration of the life-prediction model, while the Tribosystem A and B Mode II regressions (in-sample, n = 3 each) are best read as corroborating, hypothesis-generating evidence pending independent replication (Section 8.3).

Mean prediction error: 2.8% (Mode I), 1.9% (Mode II), 3.4% (Tribosystem C). Maximum single-experiment error: 7.6%. No systematic bias was observed across tribosystems. The model’s applicability requires the system to have completed running-in before W* measurement; for the three tribosystems studied, running-in lasted 15–35 min. Table 3 summarises the ξ_{TC} values and regression parameters across all three tribosystems.

Table 3
Summary of ξ_{TC} values and AE life-prediction regression parameters across all three tribosystems.

Tribosystem / Parameter	ξ_{TC} Mode I, %	ξ_{TC} Mode II, %	k (×10⁻⁸)	α	R^2
A: 12Kh2N4A–12Kh2N4A (Mode I)	0.0836–0.0941	—	1.241 ± 0.052	1.03 ± 0.04	0.978
A: 12Kh2N4A–12Kh2N4A (Mode II)	—	6.86–6.94×10⁻⁴	1.315 ± 0.018	1.01 ± 0.02	0.992[5]
B: VB23NTs–30Kh3VA (Mode II)	—	6.86–6.94×10⁻⁴	1.298 ± 0.031	1.02 ± 0.03	0.992[5]
C: 30Kh3VA + MoN–TiAlN (Mode I)	0.0836–0.0941	—	1.187 ± 0.044	1.04 ± 0.04	—[6]
C: 30Kh3VA + MoN–TiAlN (Mode II)	—	6.86–6.94×10⁻⁴	1.334 ± 0.022	1.01 ± 0.02	0.992

All confidence intervals 95%. [5]Mode II regression: n = 3 experiments for both Tribosystem A (Table 2) and Tribosystem B (preliminary; see Section 7.1 for supporting statistical indicators and limitations). ξTC Mode I range derived from Tribosystem A Table 2 data; Mode II range applies across all three tribosystems. [6]R^2 for the Tribosystem C Mode I regression is not separately tabulated in this dataset.

8. Discussion

The proposed ξ_{TC}-based approach is compared with three established AE methods in Table 4: spectral-analysis regime transitions [3], amplitude-based wear-mode discrimination [4], and derived-parameter lubrication classification [16]. None of these methods provides a thermodynamically grounded state variable together with a quantitative life-prediction capability, the combination ξ_{TC} uniquely offers.

Table 4
Comparison of the proposed ξ_{TC} dissipation-coefficient method with existing AE-based wear/lubrication-regime classification approaches.

Method	Signal feature	Physical/thermodynamic basis	Life prediction	Reported accuracy / error
Jiaa & Dornfeld [3]	AE amplitude/spectral content, 100–300 kHz	None (phenomenological)	Not provided	Qualitative regime transition only
Boness & McBride [4]	AE amplitude analysis (steel contacts)	None (phenomenological)	Not provided	Qualitative wear-mode discrimination
Strablegg et al. [16]	Direct + derived AE energy parameters	None (statistical)	Not provided	Improved lubrication-regime separability vs. amplitude stats
ML classifiers [8, 9]	AE feature vectors (clustering / SVM)	None (data-driven)	Not provided	92–95% classification accuracy
Present work (ξ_{TC})	Averaged AE power W*, applied power WL, friction coefficient μ*	Excess entropy production P[δS] [12]	Power-law model, Eqs. (1)–(3)	Mean error 2.8% (Mode I), 1.9% (Mode II), 3.4% (Tribosystem C, blind hold-out); n = 36 total

Machine learning classifiers and regression models [8, 9, 20, 21] achieve 92–97% phenomenological accuracy, but carry no physical meaning in terms of thermodynamic state and require large labelled training datasets impractical for individual tribosystem qualification. By contrast, ξ_{TC} requires only W*, W_L, and μ* — directly available from the AE hardware, load cell, and friction-torque sensor already on the test rig — and its physical basis in excess entropy production [12] gives universal applicability. The dimensionless form $\xi_{TC} = \mu^* \cdot W^* / W_L$ normalises AE power against actual frictional power, rendering the criterion independent of sensor efficiency and preamplifier gain.

Specific advantages of the proposed method: (1) continuous quantitative wear rate in physical units, detectable from first particle emission; (2) ξ_{TC} provides thermodynamic regime identification without spectral analysis; (3) life prediction in a single early-operation measurement; (4) two-order-of-magnitude sensitivity advantage over gravimetric methods; (5) applicability to anomalously low wear intensities undetectable by conventional tribometry.

8.1. Classification of Ultra-Low Wear Regimes

Based on the experimental results, two ultra-low wear friction regimes are classified by ξ_{TC}:

Mode I — Equilibrium self-organisation: ξ_{TC} = 0.0836–0.0941%. Characterised by formation of equilibrium dissipative structures stable under applied load. Dominant mechanism: reduction of activation level via secondary structure optimisation. AE signature: gradual W* stabilisation without bifurcation drop.

Mode II — Non-equilibrium self-organisation: ξ_{TC} = 6.86×10^{-4}–6.94×10^{-4}% (two orders of magnitude below Mode I). Characterised by non-equilibrium dissipative structures formed by collective ordered defect motion (rotational mesoplasticity or selective thermo-diffusion). AE signature: sharp 1–2 decade W* drop at the bifurcation point, followed by stable ultra-low plateau.

The practical consequence is that Mode II tribosystems achieve > 2× longer service life than Mode I at identical load conditions, providing a design objective for tribosystem engineering via thermal flux management or load-optimised surface coatings.

8.2. Excess Entropy Production Analysis

The excess entropy production criterion P[δS] [12] is the fundamental thermodynamic parameter governing tribosystem stability under non-equilibrium self-organisation. For Mode II operation, the stability condition $(\delta^2S)_{TS} \leq 0$ is satisfied: the non-equilibrium ordered structures (work-hardened submicron surface layer in Tribosystem A; porous Fe–Pb–Sb film in Tribosystem B) continuously export entropy to the environment, maintaining thermodynamic stability far from equilibrium under constant applied power. For Mode I (equilibrium self-organisation), $(\delta^2S)_{TS} \to 0$ after running-in, consistent with the minimum entropy production theorem [13]. This thermodynamic distinction underpins the two-order-of-magnitude separation of ξ_{TC}: the transition from $(\delta^2S)_{TS} \to 0$ (Mode I) to $(\delta^2S)_{TS} \leq 0$ (Mode II) corresponds to a sign change at the bifurcation point and is reflected directly in the measured W* drop of 1–2 decades. For Tribosystem A, ξ_{TC} declines gradually across the Mode I series (Table 2, experiments 1–10, from 0.0941% to 0.0836%) before the two-order-of-magnitude step into Mode II ($6.86–6.94\times10^{-4}$%), the quantitative AE signature of this sign change. For Tribosystem B, the load-induced porous Fe–Pb–Sb film (Section 6) drives $(\delta^2S)_{TS}$ negative at 1600 N, producing the same Mode II reduction in ξ_{TC}. Quantitative calorimetric partitioning of frictional power to determine $(\delta^2S)_{TS}$ independently of ξ_{TC} is ongoing and will be reported in a subsequent publication.

This entropy-based framing follows the degradation-entropy generation programme [41, 42]: ξ_{TC} is proposed as a practically measurable, online proxy for the sign and relative magnitude of $(\delta^2S)_{TS}$, obtainable from existing test-rig instrumentation (Section 3.2) rather than dedicated calorimetry. The correspondence asserted is qualitative (sign and order-of-magnitude) only; a quantitative proportionality in absolute entropy units awaits the calorimetric partitioning noted above.

8.3. Mechanistic Interpretation and Limitations

The results demonstrate that the bifurcation transition to the ultra-low wear regime is governed by a critical value of the controlling parameter (thermal flux or PV), beyond which the system undergoes a

non-equilibrium phase transition. Real-time AE monitoring captures this transition through the characteristic 1–2 decade drop of W*, an event invisible to conventional tribometric sensors. The universality of this AE signature across three structurally distinct tribosystems (steel–steel, bronze–steel, coated steel–steel) supports the generality of the proposed criterion.

The mesomechanical mechanisms identified metallographically are consistent with ξ_{TC} values: the work-hardened submicron surface layer in steel (blocking wear particle emission) and the self-lubricating porous Fe-Pb-Sb film in bronze (reducing real friction coefficient) both represent non-equilibrium ordered structures that export entropy and stabilise the tribosystem far below the Mode I dissipation level.

A practical implication is that the MoN–TiAlN coating architecture, by reproducing the graded structure arising from non-equilibrium self-organisation (hard elastic outer layer / compliant interlayer), deterministically drives Tribosystem C into Mode II, achieving > 2× life extension without tribosystem redesign.

For Tribosystem C, the coating-specific self-organisation pathway proposed in Section 4.1 is supported by the AE signature (Fig. 2b) and ξ_{TC} classification; direct confirmation (cross-sectional EDS, Fourier sub-block analysis, microhardness profiling of the MoN–TiAlN layer) is a priority for future work, to establish whether TiAlN redistribution or an alternative pathway governs Mode II behaviour.

Limitations: the regression coefficients k and α are tribosystem-specific, requiring per-material calibration. The Mode II regressions for Tribosystems A and B each rest on only three in-sample experiments (Section 7.2); despite converging evidence — notably the close agreement between the independently-fitted A and B coefficients (Section 7.1) — these coefficients remain preliminary pending additional replicates, especially beyond 1600 N. The ξTC Mode I/II ranges reported for Tribosystems B and C coincide with those measured for Tribosystem A (Table 2) rather than being independently derived per tribosystem; this convergence, while consistent with the claimed cross-system universality, awaits dedicated confirmation. The model assumes steady-state operation after running-in; transient loading requires additional treatment. Future work will target generalised, material-invariant AE criteria and machine-learning-assisted bifurcation-point detection from AE waveform shape.

9. Conclusions

1. 1. The AE-based wear rate measurement methodology resolves wear from the first material particle emission in information units [rel. inf. units/s], providing a two-order-of-magnitude sensitivity advantage over gravimetric methods and qualifying AE as an ultra-low wear measurement technology.
2. 2. The bifurcation transition to the ultra-low wear regime is universally characterised by a 1–2 decade drop in averaged AE power W*, detectable in real time across all three tribosystem classes investigated.

3. 3. A power-law AE life-prediction model ($I = k(W^*)^{\alpha}$) is proposed; its primary validated result is a genuine blind hold-out verification on Tribosystem C (3.4% mean error, 17 independent experiments), corroborated by consistent, in-sample regressions on Tribosystems A and B (mean error 2.8% for Mode I, 1.9% for Mode II; maximum single-experiment error ≤ 7.6% across the full 36-experiment dataset), without interrupting tribosystem operation.
4. 4. The dissipation coefficient ξ_{TC} provides a physically interpretable, instrument-agnostic criterion separating Mode I (equilibrium, ξ_{TC} = 0.0836–0.0941%) from Mode II (non-equilibrium, ξ_{TC} = 6.86×10^{-4}–6.94×10^{-4}%) ultra-low wear regimes by two orders of magnitude.
5. 5. Rotational mesoplasticity (steel 12Kh2N4A) and selective thermo-diffusion (bronze VB23NTs) are identified as mechanistically distinct non-equilibrium self-organisation pathways, confirmed by complementary Fourier sub-block analysis, EDS mapping, and microhardness profiling.
6. 6. The thermodynamic stability condition $(\delta^2S)_{TS} \leq 0$ characterises Mode II operation, consistent with the minimum entropy production theorem for Mode I ($(\delta^2S)_{TS} \to 0$), and provides a unifying framework for both regime types.

Declarations

Declaration of Competing Interest

The authors declare that they have no known competing financial interests or personal relationships that could have appeared to influence the work reported in this paper.

Funding

Declaration

The authors declare no funding sources specific to this study.

Author Contribution

V.S. conceived the study, designed and performed the experiments, developed the ξTC dissipation criterion and the AE life-prediction model, analysed the data, and wrote the manuscript. M.M. contributed to the thermodynamic analysis and interpretation, and reviewed and edited the manuscript. Both authors read and approved the final manuscript.

Acknowledgement

The authors thank the staff of the Tribology Laboratory for their experimental support. Gratitude is also extended to the Faculty of Mechanical Engineering, STU in Bratislava.

Data Availability

The experimental dataset supporting this study (36 experiments: AE time-series W*(t) and I(t), gravimetric wear mass, ξTC values) is summarised in Tables 1–4 of the main text. Additional figures (Supplementary Figs. S1–S10) and EDS compositional tables for Tribosystem B (Supplementary Tables S1–S3) are provided in the Supplementary Information accompanying this article. Raw AE waveform files and metallographic images are available from the corresponding author upon reasonable request.

References

1. Meng, Y. et al. A review of advances in tribology in 2020–2021. *Friction* **10** (10), 1443–1595. https://doi.org/10.1007/s40544-022-0685-7 (2022).
2. Feng, P. et al. A review on the relationships between acoustic emission, friction and wear in mechanical systems. *Appl. Mech. Rev.* **72** (2), 020801. https://doi.org/10.1115/1.4044799 (2020).
3. Jiaa, C. L. & Dornfeld, D. A. Experimental studies of sliding friction and wear via acoustic emission signal analysis. *Wear* **139**, 403–424. https://doi.org/10.1016/0043-1648(90)90066-N (1990).
4. Boness, R. J. & McBride, S. L. Adhesive and abrasive wear studies using acoustic emission techniques. *Wear* **149** (1–2), 41–53. https://doi.org/10.1016/0043-1648(91)90364-G (1991).
5. Rastegaev, I. A., Merson, D. L. & Vinogradov, A. Using AE signal categorization for reconstruction of wear development timeline in tribosystems. *Wear* **410–411**, 83–92. https://doi.org/10.1016/j.wear.2018.01.006 (2018).
6. Baranov, V. M., Kudryavtsev, E. M., Sarychev, G. A. & Schavelin, V. M. *Acoustic emission in friction* 291 (Elsevier, 2007).
7. Geng, Z., Puhan, D. & Reddyhoff, T. Using acoustic emission to characterize friction and wear in dry sliding steel contacts. *Tribol Int.* **134**, 394–407. https://doi.org/10.1016/j.triboint.2019.02.014 (2019).
8. He, D. et al. Acoustic emission clustering analysis for identification of wear mechanisms in sliding contact. *J. Tribol*. **142** (8), 081701. https://doi.org/10.1115/1.4046437 (2020).
9. Mokhtari, N., Pelham, J. G., Nowoisky, S., Bote-Garcia, J-L. & Gühmann, C. Friction and wear monitoring methods for journal bearings of geared turbofans based on acoustic emission signals and machine learning. *Lubricants* **8** (3), 29. https://doi.org/10.3390/lubricants8030029 (2020).
10. Hase, A., Mishina, H. & Wada, M. Correlation between features of acoustic emission signals and mechanical wear mechanisms. *Wear* **292–293**, 144–150. https://doi.org/10.1016/j.wear.2012.05.019 (2012).
11. Hase, A., Wada, M. & Mishina, H. Scanning electron microscope observation study for identification of wear mechanism using acoustic emission technique. *Tribol Int.* **72**, 51–57. https://doi.org/10.1016/j.triboint.2013.12.002 (2014).
12. Nicolis, G. & Prigogine, I. *Self-organisation in non-equilibrium systems* 491 (Wiley, 1977).

13. Prigogine, I. *Introduction to thermodynamics of irreversible processes* 3rd edn, 147 (Interscience, 1967).
14. Panin, V. E. et al. Physical mesomechanics of materials under severe plastic deformation and tribological loading. *Phys. Mesomech*. **24** (2), 121–131. https://doi.org/10.1134/S1029959921020016 (2021).
15. Klamecki, B. E. A review of friction and wear effects on acoustic emission generation. *Res. Nondestruct Eval*. **2** (3), 139–159. https://doi.org/10.1080/09349849009409619 (1990).
16. Strablegg, C., Summer, F., Renhart, P., Pusterhofer, M. & Grün, F. In-depth study of direct and derived acoustic emission parameters and their information content for classifying lubricated tribological sliding contacts. *Tribol Int.* **186**, 108651. https://doi.org/10.1016/j.triboint.2023.108651 (2023).
17. Baccar, D. & Söffker, D. Wear detection by means of wavelet-based acoustic emission analysis. *Mech. Syst. Signal. Process.* **60–61**, 198–207. https://doi.org/10.1016/j.ymssp.2015.02.006 (2015).
18. Zaporozhets, V. V. & Stadnychenko, V. N. Methodology for accelerated evaluation of wear resistance of specimens with electrospark coatings [Metodolohiia pryskorenoho otsinuvannia znosostijkosti zrazkiv z elektroiskrovymy pokryttiamy, in Ukrainian]. Probl Tribol. ;(4):25–32. (2010). Available at: https://tribology.khmnu.edu.ua
19. Voitov, V., Stadnychenko, V., Varvarov, V. & Stadnychenko, N. Mechanisms of self-organisation in tribosystems operating under conditions of abnormally low friction and wear. *Adv. Mech. Eng.* **12**, 1–14. https://doi.org/10.1177/1687814020963843 (2020).
20. Gutierrez, R., Fang, T., Mainwaring, R. & Reddyhoff, T. Predicting the coefficient of friction in a sliding contact by applying machine learning to acoustic emission data. *Friction* **12** (6), 1299–1321. https://doi.org/10.1007/s40544-023-0834-7 (2024).
21. Strablegg, C., Summer, F., Renhart, P. & Grün, F. Prediction of friction power via machine learning of acoustic emissions from a ring-on-disc rotary tribometer. *Lubricants* **11** (2), 37. https://doi.org/10.3390/lubricants11020037 (2023).
22. Olejnik, P. & Desta, Y. D. Friction-induced interactions: acoustic emissions, vibrations, and wear – a multiscale review. *Nonlinear Dyn.* **113** (18), 24101–24140. https://doi.org/10.1007/s11071-025-11397-5 (2025).
23. Lijesh, K. P. & Khonsari, M. M. A unified treatment of tribo-components degradation using thermodynamics framework: a review on adhesive wear. *Entropy* **23** (10), 1329. https://doi.org/10.3390/e23101329 (2021).
24. Gershman, I. S. et al. The conditions necessary for the formation of dissipative structures in tribo-films on friction surfaces that decrease the wear rate. *Entropy* **25** (5), 771. https://doi.org/10.3390/e25050771 (2023).
25. Heinlein, R., Grebe, M. & Herrmann, C. Detection of lubrication condition in hydrodynamic journal bearings based on dynamic experimentation using acoustic emission and machine learning. *Lubricants* **14** (6), 229. https://doi.org/10.3390/lubricants14060229 (2026).

26. Kalifa, M., Starr, A. & Khan, M. Current research and challenges in modelling wear, friction, and noise in mechanical contacts. *Proc. Inst. Mech. Eng. Part. J: J. Eng. Tribol*. **239** (8). https://doi.org/10.1177/13506501241311174 (2025).
27. Archard, J. F. Contact and Rubbing of Flat Surfaces. *J. Appl. Phys.* **24** (8), 981–988. https://doi.org/10.1063/1.1721448 (1953).
28. Cohen, J. *Statistical Power Analysis for the Behavioral Sciences* 2nd edn (Lawrence Erlbaum Associates, 1988).
29. Faul, F., Erdfelder, E., Lang, A. G. & Buchner, A. G*Power 3: A flexible statistical power analysis program for the social, behavioral, and biomedical sciences. *Behav. Res. Methods*. **39**, 175–191. https://doi.org/10.3758/BF03193146 (2007).
30. Xu, J. et al. Tribological properties of MoN/TiN multilayer coatings prepared via high-power impulse magnetron sputtering. *Lubricants* **13** (8), 319. https://doi.org/10.3390/lubricants13080319 (2025).
31. Ilie, F. Tribological behaviour of the steel/bronze friction pair (journal bearing type) functioning with selective mass transfer. *Int. J. Heat. Mass. Transf.* **124**, 655–662. https://doi.org/10.1016/j.ijheatmasstransfer.2018.03.107 (2018).
32. Trusov, P. V., Shveykin, A. I. & Kondratyev, N. S. Yants AYu. Multilevel Models in Physical Mesomechanics of Metals and Alloys: Results and Prospects. *Phys. Mesomech*. **24** (4), 391–417. https://doi.org/10.1134/S1029959921040056 (2021).
33. Fox-Rabinovich, G., Gershman, I., Goel, S. & Endrino, J. L. Control over Multi-Scale Self-Organization-Based Processes under the Extreme Tribological Conditions of Cutting through the Application of Complex Adaptive Surface-Engineered Systems. *Lubricants* **11** (3), 106. https://doi.org/10.3390/lubricants11030106 (2023).
34. Khare, A. et al. Novel Thermal Wear Simulation Approach to Model Transient Wear and Friction in Sliding Bearings. *Lubricants* **14** (8), 295. https://doi.org/10.3390/lubricants14080295 (2026).
35. Lijesh, K. P. & Khonsari, M. M. Thermodynamic characterization of fretting-induced material degradation using degradation entropy generation framework. *Wear* https://doi.org/10.1016/j.wear.2025.206341 (2025). 582–583:206341.
36. Maich, A. A., Gronsky, R. & Komvopoulos, K. Microstructure Evolution and Fretting Wear Mechanisms of Steels Undergoing Oscillatory Sliding Contact in Dry Atmosphere. *Materials* **17** (8), 1737. https://doi.org/10.3390/ma17081737 (2024).
37. Rastegaeva, I. I., Rastegaev, I. A. & Merson, D. L. Application of Cluster Analysis of Acoustic Emission Signals to Measure Wear in Sliding Friction Units. *J. Friction Wear*. **46** (6), 386–396. https://doi.org/10.3103/S1068366626700066 (2025).
38. Tian, Y., Zheng, B., Khan, M. & Yang, Y. Real-Time Prediction of Wear Morphology and Coefficient of Friction Using Acoustic Signals and Deep Neural Networks in a Tribological System. *Processes* **13** (6), 1762. https://doi.org/10.3390/pr13061762 (2025).
39. Krishnamoorthy, V., John, A. A., Bhaumik, S. & Paleu, V. Mapping Acoustic Frictional Properties of Self-Lubricating Epoxy-Coated Bearing Steel with Acoustic Emissions during Friction Test.

Technologies **12** (3), 30. https://doi.org/10.3390/technologies12030030 (2024).

40. Wang, X. et al. A Review on Tribological Wear and Corrosion Resistance of Surface Coatings on Steel Substrates. *Coatings* **15** (11), 1314. https://doi.org/10.3390/coatings15111314 (2025).
41. Bryant, M. D., Khonsari, M. M. & Ling, F. F. On the thermodynamics of degradation. *Proc. R Soc. A.* **464**, 2001–2014. https://doi.org/10.1098/rspa.2007.0371 (2008).
42. Nosonovsky, M. Entropy in tribology: in the search for applications. *Entropy* **12** (6), 1345–1390. https://doi.org/10.3390/e12061345 (2010).

Figures

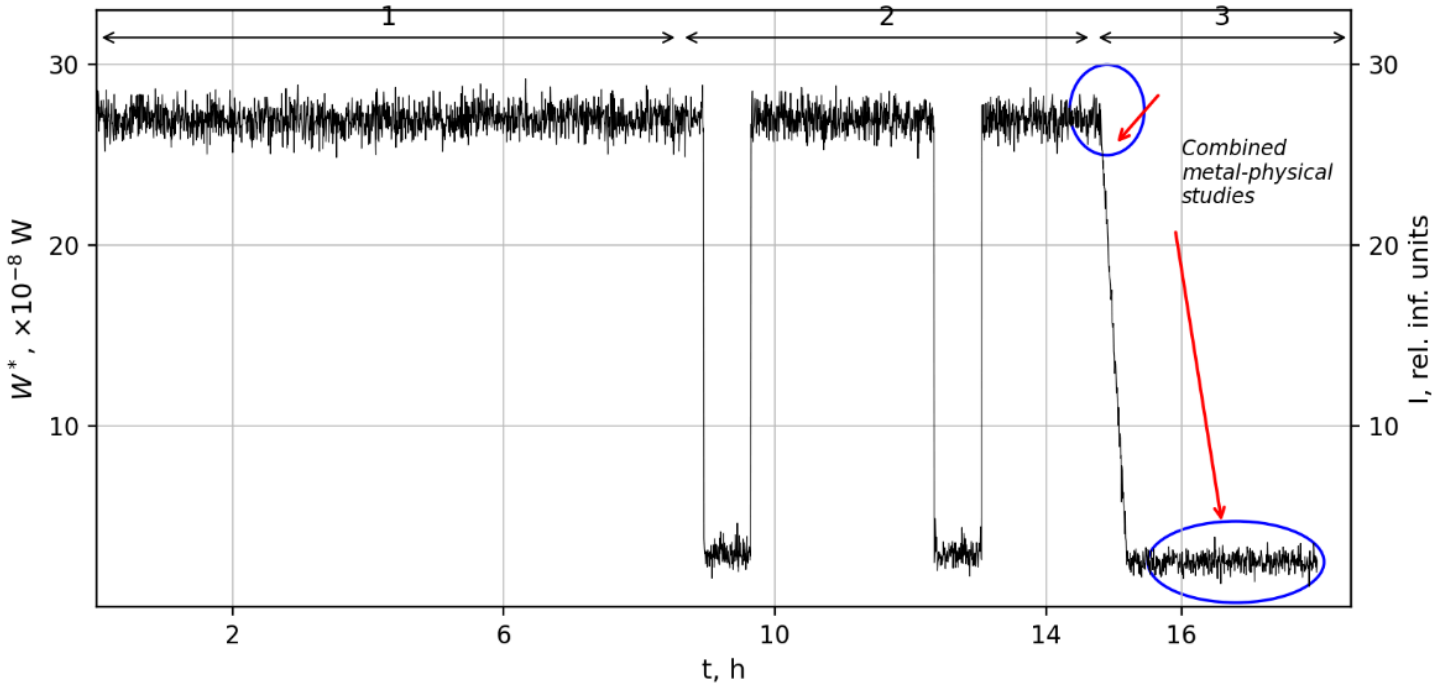


Figure 1

W* (×10⁻⁸ W, left axis) and information wear index I (rel. inf. units, right axis) versus time during transition to quasi-wearless regime. Tribosystem: disc–disc rolling with 20% sliding; 12Kh2N4A–12Kh2N4A; lubricant Б3В; load 1600 N; v = 0.5 m/s. Region 1 – steady-state wear; 2 – bifurcation point; 3 – ultra-low wear (quasi-wearless) regime.

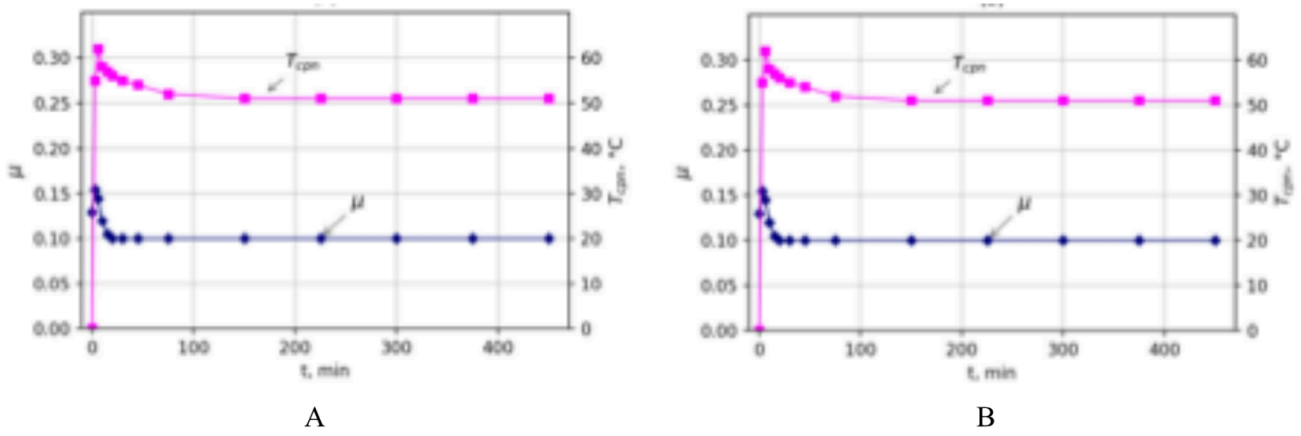


Figure 2

Tribological characteristics W* and I during ultra-low wear for Tribosystem C. Tribosystem: disc–disc rolling with 20% sliding; 30Kh3VA steel + MoN–TiAlN PVD coating; lubricant TC-1; load 1600 N; v = 0.5 m/s; PV = 3.785 W/mm². (a) Mode I (equilibrium self-organisation); (b) Mode II (non-equilibrium self-organisation). Stage 1 – latent damage accumulation; 2 – running-in; 3 – steady-state ultra-low wear.

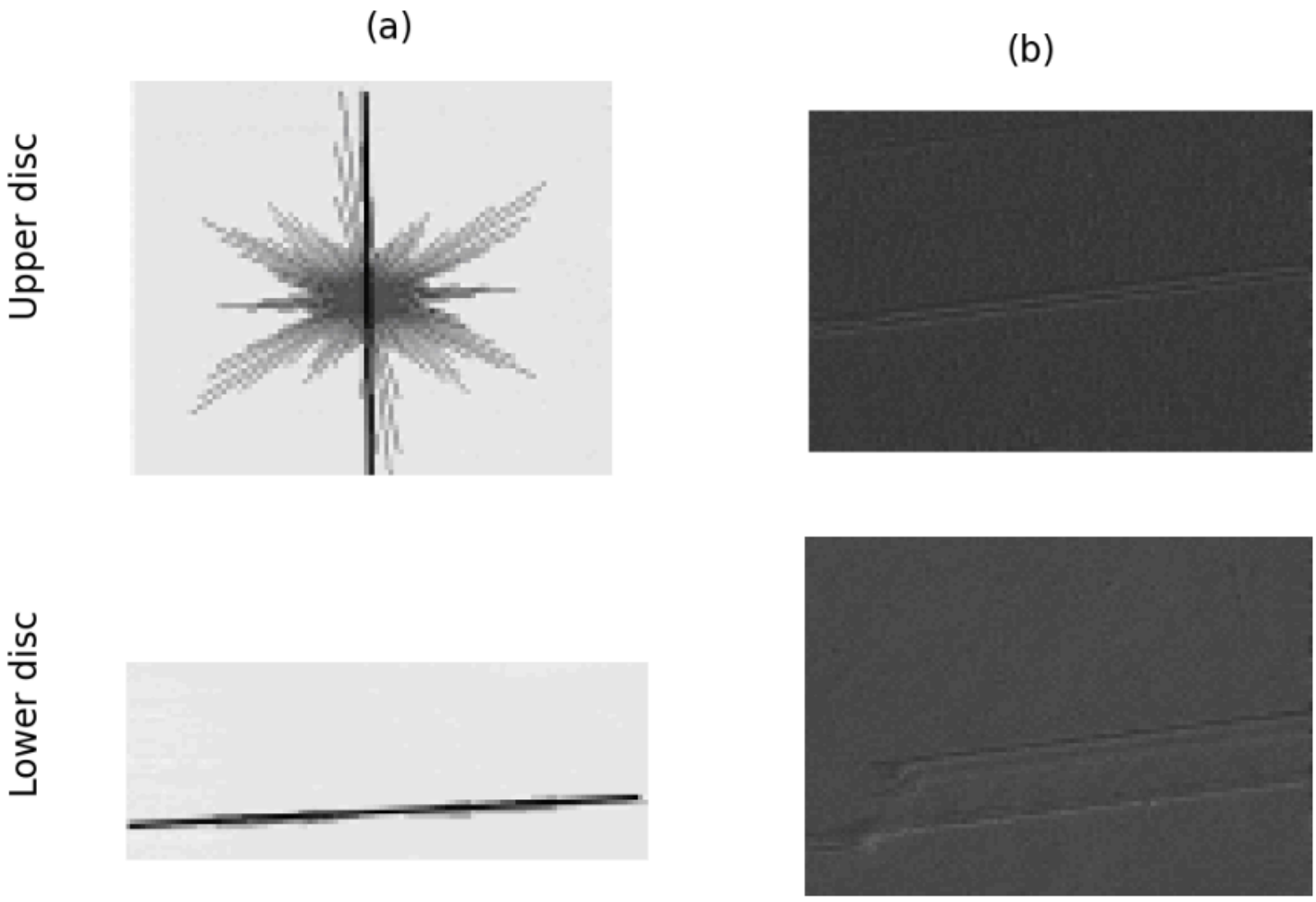


Figure 3

Fourier analysis of sub-block spatial orientation in friction surface layers at minimum wear intensity (Tribosystem A). Tribosystem: rolling with 20% sliding; 12Kh2N4A–12Kh2N4A; lubricant Б3В; load 1600 N; v = 0.5 m/s; quasi-wearless regime. (a) Sub-block orientation direction; (b) Friction surface micrographs, ×1050.

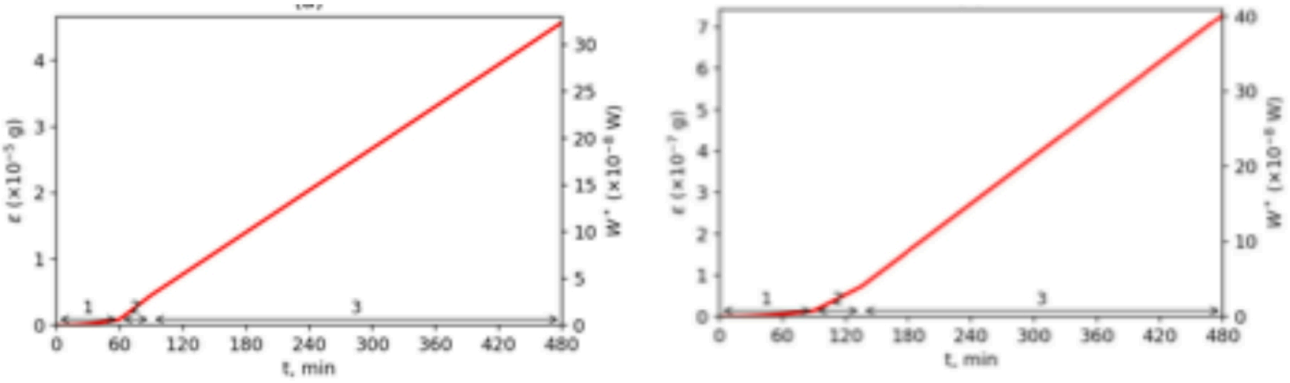


Figure 4

Cumulative wear mass ε (×10⁻⁵ g for (a), ×10⁻⁷ g for (b), left axis) and averaged AE power W* (×10⁻⁸ W, right axis) versus time on the steady-state wear section for Tribosystem C. Tribosystem: disc–disc rolling with 20% sliding; 30Kh3VA steel + MoN–TiAlN PVD coating; lubricant TC-1; load 1600 N; v = 0.5 m/s; PV = 3.785 W/mm². (a) Mode I (equilibrium self-organisation); (b) Mode II (non-equilibrium self-organisation). 1 – latent period of damage accumulation; 2 – running-in; 3 – steady-state wear, illustrating the same quasi-linear ε–W* relationship as Eq. (1) in a second tribosystem class.

Supplementary Files

This is a list of supplementary files associated with this preprint. Click to download.

- SupplementaryInformation.docx